Bulletin of the Seismological Society of America, Vol. 103, No. 4, pp. 2161–2172, August 2013, doi: 10.1785/0120120165

# Three-Dimensional Wave Gradiometry for Polarized Seismic Waves

by Christian Poppeliers and Predrag Punoševac

**Abstract** We expand the theoretical development of seismic-wave gradiometry to 3D using the polarized wavefield. First, we develop a map that relates the Cartesian spatial derivatives to the spatial derivatives in spherical coordinates. We then develop a set of partial differential equations that relate the spherical derivatives of the observed wavefield to the body-wave radiation patterns. Because the spherical derivatives of the wavefield depend on the direction of wave propagation, we also develop relationships to find the propagation direction using simple ratios of the Cartesian-based wave derivatives. Finally, we test the robustness of estimating the wave-propagation direction, and its sensitivity to noise.

## Introduction

Seismic gradiometry is a new array-processing methodology that can estimate wave slowness as well as the geometrical spreading and radiation patterns of a propagating wavefield (Langston, 2007a,b,c). Gradiometric analysis of seismic waves offers two primary advantages over conventional array processing (e.g., beam forming). First, the array used to conduct the observations must have a small aperture compared to a conventional array, making deployment and maintenance of the instrumentation much easier. The need for a small aperture array stems from the fact that the primary observables are spatial gradients of the wavefield, which can be estimated from an array so long as the array aperture is no more than 10% of the wavefield's central wavelength. The second advantage is that gradiometry provides estimates of wave slowness, geometrical spreading, and radiation patterns for a point-by-point basis on the entire seismogram.

The details of the gradiometry method are outlined in Langston (2007a,b,c). The method was extended by Poppeliers (2010) with the introduction of the wavelet transform to provide wave attributes that are a function of time and frequency. Also, by using the multiwavelet transform, Poppeliers (2011) showed that it is possible to calculate formal uncertainty estimates on the estimated wave attributes. However, all of the previous work on seismic-wave gradiometry is for 1D and 2D analysis, as would be appropriate for surface deployments of seismic arrays. The natural extension to the gradiometric method is to expand the theory and analysis to 3D. Because of the small scale required for gradiometers, a 3D deployment of a seismic gradiometer is a tractable proposition via bore-hole deployment of instruments. For example, to analyze high-frequency seismic waves from local and regional earthquakes, the gradiometer aperture would only need to be a few tens of meters assuming typical near-surface body-wave velocities and frequencies below 1–5 Hz. Another example of a potential application is in petroleum production, for which 3D gradiometry could be used to monitor hydraulic fracturing operations. In this case the high frequencies of the observed wavefield would require a gradiometer less than a meter in aperture.

Anticipating this type of array deployment, we developed the theory for 3D gradiometric analysis of scalar waves (Poppeliers *et al.*, 2013, henceforth referred to as Paper 1). Our formulation followed that of Langston (2007b) in that the 3D gradiometry problem was solved as three 1D problems for wave slowness. In Paper 1, we assumed a spherical wave model and found that the terms for geometrical spreading and radiation pattern depended on the direction of the wavefield.

The work presented here builds on that of Paper 1 except that we extend the analysis to include polarized seismic waves. We find that by including polarized waves in our analysis the gradiometry method can estimate the wave direction using simple ratios of horizontal- and vertical-component spatial wave derivatives, without the need for complicated gradiometric analysis as required in Paper 1. Additionally, we develop a set of partial differential equations that relate the radiation patterns of body waves to the spherical spatial derivatives of the observed wavefield.

## Theoretical Development

In our formulation, we center the coordinate system at the seismic origin. We further assume that the wavefield is perfectly spherical. The wavefield is recorded by a 3D array of three-component seismometers that are oriented in the conventional manner (i.e., east $\hat{i}$, north $\hat{j}$, and vertical $\hat{k}$). We use $x_i$, $i = 1, 2, 3$ to denote coordinates in the corresponding directions $\hat{i}$, $\hat{j}$, and $\hat{k}$, respectively (Fig. 1). However, the problem is most conveniently cast in spherical coordinates. We define the unit vectors for the spherical coordinate system as $\hat{r}$, $\hat{\phi}$, and $\hat{\theta}$, or so-called ray coordinates in seismology. Radial motion due to the passage of a *P* wave

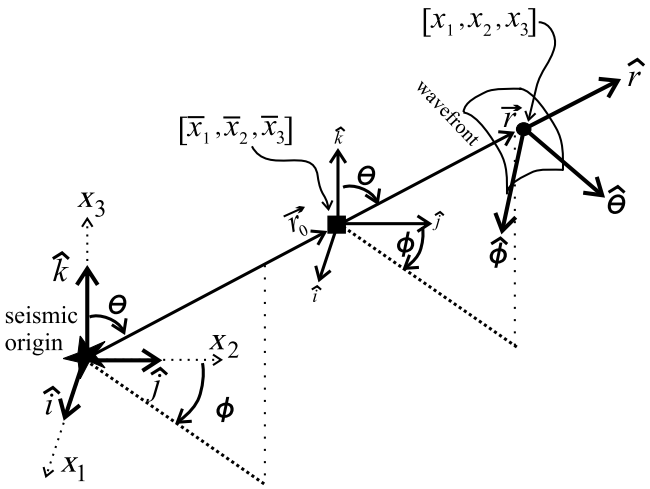


**Figure 1.** Definition of the coordinate systems and the angles. The coordinate axes are centered on the seismic origin. The dashed axes denote the Cartesian frame by which we observe the seismograms, which is in the natural coordinate system of the seismic array (e.g., $x_1$, $x_2$, and $x_3$), with unit vectors $\hat{i}$, $\hat{j}$, and $\hat{k}$. The spherical coordinates that are most natural to the wave itself (e.g., ray coordinates) are indicated by the unit vectors $\hat{r}$,$\hat{\theta}$, and $\hat{\phi}$. The vector from the seismic source to the array center is $\vec{r}_0$ and the distance from the seismic source to the point on the wavefront along $\hat{r}$ is $r$. The array center is located at $[\bar{x}_1, \bar{x}_2, \bar{x}_3]$ and the point described by $\vec{r}$ is $[x_1, x_2, x_3]$.

is denoted as $u_r$. Transverse motion associated with an $SH$ wave is $u_\phi$, and the transverse motion from an $SV$ wave is $u_\theta$.

We assume a spherical wave model based on the form of a propagating wave solution of a point source in a homogeneous medium. Our model assumes that the wave is approximately planar over the scale of the array which is centered at $[\bar{x}_1, \bar{x}_2, \bar{x}_3]$, but still includes the effects of geometrical spreading and radiation patterns. Assuming a point source at some depth, the radial and transverse displacements observed at the location relative to the source $(r, \phi, \theta)$ are given as

$$\begin{aligned} u_r(r,\phi,\theta) &= G_P(r)\Re_P(\phi,\theta) f_P[t - |\vec{p}_P|(r)(r-r_0)] \\ u_\phi(r,\phi,\theta) &= G_{SH}(r)\Re_{SH}(\phi,\theta) f_{SH}[t - |\vec{p}_{SH}|(r)(r-r_0)] \\ u_\theta(r,\phi,\theta) &= G_{SV}(r)\Re_{SV}(\phi,\theta) f_{SV}[t - |\vec{p}_{SV}|(r)(r-r_0)], \end{aligned} \tag{1}$$

in which subscripts denote the component of displacement, $r = |\vec{r}|$ is the distance along the vector $\vec{r}$ from the seismic source to the point on the wavefront in the direction along the unit vector $\hat{r}$, $r_0 = |\vec{r}_0|$ is the distance from the source to the array center along the unit vector $\hat{r}$, and $r - r_0$ is the distance from the center of the array to the wavefront along $\hat{r}$. Note that the $P$ wave is polarized in the radial direction, whereas the $S$ wave can be mixed in the $\phi$ and $\theta$ directions, yielding both $SH$ and $SV$ waves, respectively. The geometrical spreading $G$, radiation pattern $\Re$, and slowness $\vec{p}$ are indicated for each wave type (either $P$, $SH$, or $SV$) by the corresponding subscript. Also, the scalar quantity $|\vec{p}|$ for each wave type is the inverse wavespeed along the radial direction. This model honors the fact that $P$ and $S$ waves travel at different speeds as well as the possibility that shear-wavespeeds and radiation patterns may depend on polarization direction (e.g., shear-wave splitting).

If the direction of propagation is known, the spherical spatial gradients of the waves in equation (1) can be derived using the chain rule of calculus:

$$\begin{bmatrix} u_{r,r} \\ u_{r,\phi} \\ u_{r,\theta} \\ u_{\phi,r} \\ u_{\phi,\phi} \\ u_{\phi,\theta} \\ u_{\theta,r} \\ u_{\theta,\phi} \\ u_{\theta,\theta} \end{bmatrix} = \begin{bmatrix} A_P & B_P & 0 & 0 & 0 & 0 \\ \frac{1}{\Re_P}\frac{\partial \Re_P}{\partial \phi} & 0 & 0 & 0 & 0 & 0 \\ \frac{1}{\Re_P}\frac{\partial \Re_P}{\partial \theta} & 0 & 0 & 0 & 0 & 0 \\ 0 & 0 & A_{SH} & B_{SH} & 0 & 0 \\ 0 & 0 & \frac{1}{\Re_{SH}}\frac{\partial \Re_{SH}}{\partial \phi} & 0 & 0 & 0 \\ 0 & 0 & \frac{1}{\Re_{SH}}\frac{\partial \Re_{SH}}{\partial \theta} & 0 & 0 & 0 \\ 0 & 0 & 0 & 0 & A_{SV} & B_{SV} \\ 0 & 0 & 0 & 0 & \frac{1}{\Re_{SV}}\frac{\partial \Re_{SV}}{\partial \phi} & 0 \\ 0 & 0 & 0 & 0 & \frac{1}{\Re_{SV}}\frac{\partial \Re_{SV}}{\partial \theta} & 0 \end{bmatrix} \begin{bmatrix} u_r \\ \dot{u}_r \\ u_\phi \\ \dot{u}_\phi \\ u_\theta \\ \dot{u}_\theta \end{bmatrix}, \tag{2}$$

for which the first index denotes the wave component and the second index indicates partial derivative in the given direction. For example $u_{r,r} = \frac{\partial u_r}{\partial r}$ denotes partial derivative of radial component in the radial direction. The coefficients in the matrix are

$$A_i = \frac{1}{G_i}\frac{\partial G_i}{\partial r}, \tag{3}$$

and

$$B_i = -p_i - \frac{\partial p_i}{\partial r}(r - r_0), \tag{4}$$

for which $i = P, SH, SV$ indicates the wave type of interest. Equation (2) relates the wave gradients to wave velocity and radiation patterns. From equation (2) we obtain

$$\frac{u_{r,\phi}}{u_{r,\theta}} = \frac{\frac{\partial \Re_P}{\partial \phi}}{\frac{\partial \Re_P}{\partial \theta}}, \tag{5}$$

$$\frac{u_{\phi,\phi}}{u_{\phi,\theta}} = \frac{\frac{\partial \Re_{SH}}{\partial \phi}}{\frac{\partial \Re_{SH}}{\partial \theta}}, \tag{6}$$

and

$$\frac{u_{\theta,\phi}}{u_{\theta,\theta}} = \frac{\frac{\partial \Re_{SV}}{\partial \phi}}{\frac{\partial \Re_{SV}}{\partial \theta}}. \tag{7}$$

Equations (5) through (7) relate the spherical radiation patterns for all three body-wave types to the wavefield's spherical spatial derivatives. The caveat is that the wavefield derivatives must be estimated in spherical coordinates, despite the actual observations being in Cartesian coordinates.

Thus, the first problem to be solved is to estimate the spherical wavefield derivatives from the Cartesian observations. For this to be possible, we require knowledge of the propagation direction at the observation point. Therefore, in the next section we will develop (1) a relationship between the Cartesian observations and the spherical derivatives and (2) a method to estimate the wave direction from the same Cartesian observations.

We note that the model of wave propagation that we use is a first-order approximation: a perfectly spherical wave in a homogeneous medium. Ultimately, the physics of actual wave propagation in a heterogeneous Earth are much more complicated than the mathematics that we use to describe it. The point of gradiometric analysis is to estimate various wave parameters for each point along a seismogram for which the wave parameters can vary in time. Thus, the easiest way to reconcile the source-centered coordinate system and spherical waves with time-variable wave parameters is to think of the source as changing location with time. Physically, this can be due to seismic scattering, for which each arrival has a different origin, or a finite rupture fault, for which each arrival on the seismogram has a different physical source location.

### Estimating Spherical Derivatives and Wave Direction from Cartesian Observations

The relationship between the Cartesian and spherical coordinates is given by

$$x_1 = r\sin\theta\sin\phi \qquad x_2 = r\sin\theta\cos\phi \qquad x_3 = r\cos\theta\,, \tag{8}$$

where the angle $\phi$ is measured from $\hat{j}$ in clockwise direction (following seismology conventions) and the angle $\theta$ is measured from $\hat{k}$ downwards (Fig. 1).

We now use $\phi$, $\theta$ as Euler angles to relate the Cartesian coordinate system to the corresponding spherical coordinate system. Note that these coordinate systems are both centered at the seismic source. To transform Cartesian base vectors $\hat{i}$, $\hat{j}$, $\hat{k}$ into the spherical base vectors $\hat{r}$, $\hat{\phi}$, $\hat{\theta}$ we use two rotations. Although the rotation of seismograms from Cartesian coordinates to ray coordinates is well known, we write the two rotations explicitly, as it makes the derivation of the derivatives much more clear. The first rotation is about the $\hat{k}$ axis in the counter-clockwise direction for the angle $\frac{\pi}{2}-\phi$ and given by the matrix of rotation

$$\begin{aligned}\mathbf{R}_\phi &= \begin{bmatrix} \cos(\frac{\pi}{2}-\phi) & -\sin(\frac{\pi}{2}-\phi) & 0 \\ \sin(\frac{\pi}{2}-\phi) & \cos(\frac{\pi}{2}-\phi) & 0 \\ 0 & 0 & 1 \end{bmatrix} \\ &= \begin{bmatrix} \sin\phi & -\cos\phi & 0 \\ \cos\phi & \sin\phi & 0 \\ 0 & 0 & 1 \end{bmatrix}. \end{aligned} \tag{9}$$

The rotation in equation (9) is followed by a rotation $\theta$:

$$\mathbf{R}_\theta = \begin{bmatrix} \cos\theta & 0 & -\sin\theta \\ 0 & 1 & 0 \\ \sin\theta & 0 & \cos\theta \end{bmatrix}. \tag{10}$$

Because matrices $\mathbf{R}_\phi$ and $\mathbf{R}_\theta$ are rotations, they are non-singular and orthogonal, but not commutative (i.e., $\mathbf{R}_\phi^{-1} = \mathbf{R}_\phi^T$ and $\mathbf{R}_\theta^{-1} = \mathbf{R}_\theta^T$). Combining the matrices $\mathbf{R}_\phi$ and $\mathbf{R}_\theta$ gives the map from the Cartesian frame base vectors to the ray-based frame base vectors:

$$\begin{bmatrix} \hat{r} \\ \hat{\phi} \\ \hat{\theta} \end{bmatrix} = \mathbf{R}_\theta\mathbf{R}_\phi \begin{bmatrix} \hat{i} \\ \hat{j} \\ \hat{k} \end{bmatrix}. \tag{11}$$

We use equation (11) to derive a relation between the wave displacement $u_1(x_1, x_2, x_3)$, $u_2(x_1, x_2, x_3)$, and $u_3(x_1, x_2, x_3)$ in Cartesian and spherical coordinates. Given an arbitrary displacement vector $\vec{v}$, we can write

$$\vec{v} = [\,u_1 u_2 u_3\,] \begin{bmatrix} \hat{i} \\ \hat{j} \\ \hat{k} \end{bmatrix} \tag{12}$$

or

$$\vec{v} = [\,u_r u_\phi u_\theta\,] \begin{bmatrix} \hat{r} \\ \hat{\phi} \\ \hat{\theta} \end{bmatrix}. \tag{13}$$

Substituting equation (11) into equation (13) we obtain

$$\vec{v} = [\,u_r u_\phi u_\theta\,]\mathbf{R}_\theta\mathbf{R}_\phi \begin{bmatrix} \hat{i} \\ \hat{j} \\ \hat{k} \end{bmatrix}. \tag{14}$$

Combining equations (14) and (12) we obtain

$$[\,u_r u_\phi u_\theta\,]\mathbf{R}_\theta\mathbf{R}_\phi = [\,u_1 u_2 u_3\,], \tag{15}$$

or equivalently

$$[\,u_r u_\phi u_\theta\,] = [\,u_1 u_2 u_3\,]\mathbf{R}_\phi^{-1}\mathbf{R}_\theta^{-1}, \tag{16}$$

which, due to orthogonality of rotation matrices, can be also written as

$$[\,u_r u_\phi u_\theta\,] = [\,u_1 u_2 u_3\,]\mathbf{R}_\phi^T\mathbf{R}_\theta^T. \tag{17}$$

Finally, we use the facts that $(A^T)^T = A$ and $(AB)^T = B^T A^T$ to write equation (17) as

$$\begin{bmatrix} u_r \\ u_\phi \\ u_\theta \end{bmatrix} = \mathbf{R}_\theta\mathbf{R}_\phi \begin{bmatrix} u_1 \\ u_2 \\ u_3 \end{bmatrix}, \tag{18}$$

which produces the mapping we were seeking.

Now we compute the derivatives with respect to $r$, $\phi$, and $\theta$. Using the chain rule on equation (18) we obtain

$$\begin{bmatrix} u_{r,r} \\ u_{\phi,r} \\ u_{\theta,r} \end{bmatrix} = \mathbf{R}_\theta \mathbf{R}_\phi \begin{bmatrix} u_{1,1} & u_{1,2} & u_{1,3} \\ u_{2,1} & u_{2,2} & u_{2,3} \\ u_{3,1} & u_{3,2} & u_{3,3} \end{bmatrix} \begin{bmatrix} \sin\phi \sin\theta \\ \cos\phi \sin\theta \\ \cos\theta \end{bmatrix} \quad (19)$$

(see the Appendix for the derivation of the derivatives). For notational efficiency, we use indicial notation to represent partial derivatives (i.e., $u_{i,j} = \frac{\partial u_i}{\partial x_j}$). Likewise, the derivative with respect to $\phi$ is

$$\begin{bmatrix} u_{r,\phi} \\ u_{\phi,\phi} \\ u_{\theta,\phi} \end{bmatrix} = \mathbf{R}_\theta \begin{bmatrix} \cos\phi & \sin\phi & 0 \\ -\sin\phi & \cos\phi & 0 \\ 0 & 0 & 0 \end{bmatrix} \begin{bmatrix} u_1 \\ u_2 \\ u_3 \end{bmatrix} + \mathbf{R}_\theta \mathbf{R}_\phi \begin{bmatrix} u_{1,1} & u_{1,2} & u_{1,3} \\ u_{2,1} & u_{2,2} & u_{2,3} \\ u_{3,1} & u_{3,2} & u_{3,3} \end{bmatrix} \begin{bmatrix} r\cos\phi \sin\theta \\ -r\sin\phi \sin\theta \\ 0 \end{bmatrix} \quad (20)$$

and the partial derivatives with respect to $\theta$ are

$$\begin{bmatrix} u_{r,\theta} \\ u_{\phi,\theta} \\ u_{\theta,\theta} \end{bmatrix} = \begin{bmatrix} -\sin\theta & 0 & -\cos\theta \\ 0 & 0 & 0 \\ \cos\theta & 0 & -\sin\theta \end{bmatrix} \mathbf{R}_\phi \begin{bmatrix} u_1 \\ u_2 \\ u_3 \end{bmatrix} + \mathbf{R}_\theta \mathbf{R}_\phi \begin{bmatrix} u_{1,1} & u_{1,2} & u_{1,3} \\ u_{2,1} & u_{2,2} & u_{2,3} \\ u_{3,1} & u_{3,2} & u_{3,3} \end{bmatrix} \begin{bmatrix} r\sin\phi \cos\theta \\ r\cos\phi \cos\theta \\ -r\sin\theta \end{bmatrix}. \quad (21)$$

Equations (19) through (21) give us a map from the Cartesian-based observations (and the resulting Cartesian spatial derivatives) to the ray-based spherical derivatives, and are among the main results of this paper. The main motivation of deriving equations (19) through (21) is that the spherical derivatives of the wavefield are required in order to estimate the radiation patterns (equations 5–7). An additional potential application of the wavefield's spherical derivatives is the estimation of ray-based rotational motions, which we will address later in this paper.

However, before we can use equations (19) through (21), we must determine the direction of the wavefield $\theta$, $\phi$. We can do this by assuming that we are observing the wave in the far field. Under the far-field assumption, we can multiply both sides of equation (20) by $1/r$ where $r \to \infty$. This gives us

$$\frac{1}{r}\begin{bmatrix} u_{r,\phi} \\ u_{\phi,\phi} \\ u_{\theta,\phi} \end{bmatrix} = \mathbf{R}_\theta \mathbf{R}_\phi \begin{bmatrix} u_{1,1} & u_{1,2} & u_{1,3} \\ u_{2,1} & u_{2,2} & u_{2,3} \\ u_{3,1} & u_{3,2} & u_{3,3} \end{bmatrix} \begin{bmatrix} \cos\phi \sin\theta \\ -\sin\phi \sin\theta \\ 0 \end{bmatrix}. \quad (22)$$

Note that for now, we will leave the $1/r$ term on the left side of equation (22) for clarity. Similarly, the far-field spherical derivatives with respect to $\theta$ are

$$\frac{1}{r}\begin{bmatrix} u_{r,\theta} \\ u_{\phi,\theta} \\ u_{\theta,\theta} \end{bmatrix} = \mathbf{R}_\theta \mathbf{R}_\phi \begin{bmatrix} u_{1,1} & u_{1,2} & u_{1,3} \\ u_{2,1} & u_{2,2} & u_{2,3} \\ u_{3,1} & u_{3,2} & u_{3,3} \end{bmatrix} \begin{bmatrix} \sin\phi \cos\theta \\ \cos\phi \cos\theta \\ -\sin\theta \end{bmatrix}. \quad (23)$$

In the far field, radiation patterns across a gradiometer cell will be much smaller than the radial changes of the wave field, which include wave slowness. In this case, the derivatives with respect to $\theta$ and $\phi$ are essentially zero. Furthermore, because we make the approximation that $1/r \to 0$, equations (22) and (23) become

$$\begin{bmatrix} 0 \\ 0 \\ 0 \end{bmatrix} = \mathbf{R}_\theta \mathbf{R}_\phi \begin{bmatrix} u_{1,1} & u_{1,2} & u_{1,3} \\ u_{2,1} & u_{2,2} & u_{2,3} \\ u_{3,1} & u_{3,2} & u_{3,3} \end{bmatrix} \begin{bmatrix} \cos\phi \sin\theta \\ -\sin\phi \sin\theta \\ 0 \end{bmatrix} \quad (24)$$

and

$$\begin{bmatrix} 0 \\ 0 \\ 0 \end{bmatrix} = \mathbf{R}_\theta \mathbf{R}_\phi \begin{bmatrix} u_{1,1} & u_{1,2} & u_{1,3} \\ u_{2,1} & u_{2,2} & u_{2,3} \\ u_{3,1} & u_{3,2} & u_{3,3} \end{bmatrix} \begin{bmatrix} \sin\phi \cos\theta \\ \cos\phi \cos\theta \\ -\sin\theta \end{bmatrix}. \quad (25)$$

Because the matrices $\mathbf{R}_\phi$ and $\mathbf{R}_\theta$ are invertible, equations (22) and (23) can further reduce to

$$\begin{bmatrix} 0 \\ 0 \\ 0 \end{bmatrix} = \begin{bmatrix} u_{1,1} & u_{1,2} & u_{1,3} \\ u_{2,1} & u_{2,2} & u_{2,3} \\ u_{3,1} & u_{3,2} & u_{3,3} \end{bmatrix} \begin{bmatrix} \cos\phi \sin\theta \\ -\sin\phi \sin\theta \\ 0 \end{bmatrix} \quad (26)$$

and

$$\begin{bmatrix} 0 \\ 0 \\ 0 \end{bmatrix} = \begin{bmatrix} u_{1,1} & u_{1,2} & u_{1,3} \\ u_{2,1} & u_{2,2} & u_{2,3} \\ u_{3,1} & u_{3,2} & u_{3,3} \end{bmatrix} \begin{bmatrix} \sin\phi \cos\theta \\ \cos\phi \cos\theta \\ -\sin\theta \end{bmatrix} \quad (27)$$

by multiplying both sides of (22) and (23) from the left by $\mathbf{R}_\theta^{-1}$ and then by $\mathbf{R}_\phi^{-1}$.

By combining the first row of equations (19), (27), and (26) we obtain a map between the Cartesian and spherical derivatives in the far field:

$$\begin{bmatrix} u_{r,r} \\ 0 \\ 0 \end{bmatrix} = \begin{bmatrix} \sin\phi \sin\theta & \cos\phi \sin\theta & \cos\theta \\ \sin\phi \cos\theta & \cos\phi \cos\theta & -\sin\theta \\ \cos\phi \sin\theta & -\sin\phi \sin\theta & 0 \end{bmatrix} \begin{bmatrix} u_{i,1} \\ u_{i,2} \\ u_{i,3} \end{bmatrix}, \quad i = 1,2,3 \quad (28)$$

for which the mapping

$$\mathbf{U} = \begin{bmatrix} \sin\phi \sin\theta & \cos\phi \sin\theta & \cos\theta \\ \sin\phi \cos\theta & \cos\phi \cos\theta & -\sin\theta \\ \cos\phi \sin\theta & -\sin\phi \sin\theta & 0 \end{bmatrix} \quad (29)$$

has the inverse of

$$\mathbf{U}^{-1} = \begin{bmatrix} \sin\phi\sin\theta & \sin\phi\cos\theta & \cos\phi\csc\theta \\ \cos\phi\sin\theta & \cos\phi\cos\theta & -\sin\phi\csc\theta \\ \cos\theta & -\sin\theta & 0. \end{bmatrix}. \quad (30)$$

Because **U** is invertible, equation (28) can also be written as

$$\begin{bmatrix} u_{i,1} \\ u_{i,2} \\ u_{i,3} \end{bmatrix} = \begin{bmatrix} \sin\phi\sin\theta & \sin\phi\cos\theta & \cos\phi\csc\theta \\ \cos\phi\sin\theta & \cos\phi\cos\theta & -\sin\phi\csc\theta \\ \cos\theta & -\sin\theta & 0 \end{bmatrix} \begin{bmatrix} u_{r,r} \\ 0 \\ 0 \end{bmatrix}, \quad i = 1,2,3. \quad (31)$$

Note that equation (31) is actually three systems of $3 \times 3$ equations, one for each wave component $i$.

Examination of equation (31) yields the wave direction $\theta$ and $\phi$. For example, by multiplying matrices we get

$$\frac{u_{i,1}}{u_{i,2}} = \frac{u_{r,r}\sin\phi\sin\theta}{u_{r,r}\cos\phi\sin\theta} = \tan\phi, \qquad i = 1,2,3, \quad (32)$$

so we can obtain the propagation direction $\phi$ via simple division of any of the three-component Cartesian horizontal derivatives. Likewise,

$$\frac{u_{i,1}}{u_{i,3}} = \frac{u_{r,r}\sin\phi\sin\theta}{u_{r,r}\cos\theta} = \sin\phi\tan\theta, \qquad i = 1,2,3 \quad (33)$$

and

$$\frac{u_{i,2}}{u_{i,3}} = \frac{u_{r,r}\cos\phi\sin\theta}{u_{r,r}\cos\phi} = \cos\phi\tan\theta, \qquad i = 1,2,3 \quad (34)$$

gives us the wave direction $\theta$.

Thus, we obtain a result very similar to that obtained by Langston and Liang (2008) in that propagation direction can be simply obtained via the ratio of Cartesian derivatives. Beginning with equation (22), we have shown that the wave direction can be obtained by taking a ratio of the wave's Cartesian spatial derivatives as estimated from any of the three components of observed particle motion. Although not a major point, we note that equations (32) through (34), which can be obtained from equations (19) through (21) under the far-field assumption, represent a significant result of this paper.

The wave direction can also be obtained by a geometrical interpretation of spherical coordinates, but we present equations (32) through (34) as they fall naturally out of the mapping from the Cartesian to spherical derivatives. The main point of this paper is actually the mapping between the Cartesian observations and the spherical derivatives of the wavefield, and the partial differential equations (5) through (7) relating the radiation patterns to the spherical derivatives, which we will briefly discuss in the next section.

Radiation Patterns

Rewriting equations (5) through (7) gives

$$u_{r,\phi}\frac{\partial\Re_P}{\partial\theta} - u_{r,\theta}\frac{\partial\Re_P}{\partial\phi} = 0, \quad (35)$$

$$u_{\phi,\phi}\frac{\partial\Re_{SH}}{\partial\theta} - u_{\phi,\theta}\frac{\partial\Re_{SH}}{\partial\phi} = 0, \quad (36)$$

and

$$u_{\theta,\phi}\frac{\partial\Re_{SV}}{\partial\theta} - u_{\theta,\theta}\frac{\partial\Re_{SV}}{\partial\phi} = 0, \quad (37)$$

which relate the spatial changes in the wave amplitude along the $\theta$ and $\phi$ directions for a given wave type to the waves' spatial derivatives. The spherical (ray-based) derivatives are obtained from the Cartesian observations by the mappings in equations (19) through (21).

In principle, it is possible to solve equations (35) through (37) numerically. For example, one could set up a system of equations for which the radiation patterns $\Re_P$, $\Re_{SH}$, $\Re_{SV}$ are determined for a range of spatial locations. One could then fit assumed radiation patterns to the observed data and solve for the parameters of the moment tensor in a least-squares sense. However, unless the wavefield is sampled at numerous locations (and hence $\phi$, $\theta$), and unless there is an appreciable change in wave amplitude over the scale of the array, the problem would be extremely ill posed. Therefore, we anticipate that the estimation of the radiation patterns would require (1) that the recording arrays be close enough to the source so that observable amplitude changes occur over the scale of the array and (2) that the wavefield be sampled in several locations surrounding the seismic source, which would require several gradiometers surrounding the source.

The numerical solution to equations (35) through (37) is not trivial and ultimately depends on accurate estimations of the wave direction (which are required to estimate the spherical derivatives). Therefore, it is important that our method of estimating propagation direction is robust. In Paper 1, we presented a more complex method of estimating $\phi$ and $\theta$ than equations (32) and (34) and performed tests to determine the sensitivity of these methods to noise. We will take a similar approach here, and test the robustness of equations (32) and (34) and their sensitivity to noise. We leave the estimation of the actual radiation patterns to a forthcoming paper.

## Estimating Wave Direction: Numerical Verification

The goal of this section is to describe the method of estimating the wave direction from collocated, three-component, Cartesian observations. First, we outline the method of estimating the Cartesian spatial derivatives and then use equations (32) through (34) to estimate the known wave directions $\phi$, $\theta$.

### Estimating Numerical Derivatives

The first data processing step in wave gradiometry is the numerical estimation of wave derivatives for each time point in a set of seismograms. Previous researchers have used a finite-difference scheme (e.g., Bodin *et al.*, 1997; Gomberg *et al.*, 1999; Langston, 2007b); however, this requires that the array geometry and station distribution be uniform. We prefer a more generalized approach that can be used on arrays with nonuniform station distributions. Specifically, given $N$ seismic stations in a 3D array, we compute the spatial gradient $u_{i,j}$ in direction $j = 1, 2, 3$ for wave component $i = 1, 2, 3$ at location $\vec{r}_k = [x_1^{\{k\}}, x_2^{\{k\}}, x_3^{\{k\}}]$ relative to the master station $\vec{r}_0 = [x_1^{\{0\}}, x_2^{\{0\}}, x_3^{\{0\}}]$ by expanding the Taylor series:

$$\begin{aligned} du_i^{\{k\}} &= u_i^{\{k\}} - u_i^{\{0\}} \\ &= \delta x_1^{\{k\}} \frac{\partial u_i}{\partial x_1}\bigg|_{\vec{r}_0} + \delta x_2^{\{k\}} \frac{\partial u_i}{\partial x_2}\bigg|_{\vec{r}_0} + \delta x_3^{\{k\}} \frac{\partial u_i}{\partial x_3}\bigg|_{\vec{r}_0} + (du_{\text{err}}^{\{k\}})_i, \end{aligned} \tag{38}$$

for which $\delta x_i^{\{k\}} = x_i^{\{k\}} - x_i^{\{0\}}$, $i = 1, 2, 3$ and the time dependence of the seismograms is implied. Neglecting the error term, we can rewrite equation (38) as a matrix equation:

$$\begin{bmatrix} u_i^{\{1\}} - u_i^{\{0\}} \\ u_i^{\{2\}} - u_i^{\{0\}} \\ \vdots \\ u_i^{\{N\}} - u_i^{\{0\}} \end{bmatrix} = \begin{bmatrix} \delta x_1^{\{1\}} & \delta x_2^{\{1\}} & \delta x_3^{\{1\}} \\ \delta x_1^{\{2\}} & \delta x_2^{\{2\}} & \delta x_3^{\{2\}} \\ \vdots & \vdots & \vdots \\ \delta x_1^{\{N\}} & \delta x_2^{\{N\}} & \delta x_3^{\{N\}} \end{bmatrix} \begin{bmatrix} \frac{\partial u_i}{\partial x_1} \\ \frac{\partial u_i}{\partial x_2} \\ \frac{\partial u_i}{\partial x_3} \end{bmatrix}. \tag{39}$$

The term on the left is a vector containing the waveform variations for component $u_i$, $i = 1, 2, 3$ relative to the master station, the $3 \times N$ matrix contains the gradiometer geometry, and the $1 \times 3$ vector on the right contains the spatial gradients for the given component $i$. By solving equation (39) via standard matrix inversion techniques we obtain the spatial derivatives of the wavefield for all time points and components. The advantage of this approach is that the station spacing can be nonuniform and an arbitrary number of stations can be used, so long as the array is 3D in its structure. An additional advantage of this method is that the effects of spurious station amplitudes can be minimized by using a weighted least-squares solution, for which the station weights could be based on, for example, an individual station's signal-to-noise ratio.

### Synthetic Signal

To conduct the test, we constructed a virtual 15-element cubic array of three-component sensors, for which we placed a station at each corner of the cube, the center of each cube face, and one station in the approximate center of the array. We numerically propagate a wave of the form

$$\begin{aligned} u_i(t, x_1^{\{k\}}, x_2^{\{k\}}, x_3^{\{k\}}) = \frac{\Re_w}{|\vec{r}_k|} f[t - x_1^{\{k\}} p(x_1) - x_2^{\{k\}} p(x_2) \\ - x_3^{\{k\}} p(x_3)], \end{aligned} \tag{40}$$

in which $u_i$ is a simulated three-component seismogram with components $i = 1, 2, 3$, $(x_1^{\{k\}}, x_2^{\{k\}}, x_3^{\{k\}})$ is the $k$th station's array coordinates, $|\vec{r}_k|$ is the distance between the seismic source and seismic station $k$, and $p(x_1)$, $p(x_2)$, $p(x_3)$ are the (potentially time-varying) wave slownesses in the $x_1$, $x_2$, and $x_3$ directions, respectively. For our tests, we placed the array 200 km from the source; however, we found that the actual distance between the source and the array had very little effect on the estimates of the wave direction. For completeness, we computed radiation patterns $\Re_w$, $w = P, SH, SV$, for the synthetic wavefield; however, we found that for our tests we obtained nearly identical results for wave direction regardless of the form of $\Re$. The geometrical spreading is assumed to be identical for all three wave types and is a simple $\frac{1}{r}$ relationship.

The function given by equation (40) simulates a wave traveling through an infinite three-space with geometrical spreading and radiation patterns. For this work, we define $p(x_1)$, $p(x_2)$, $p(x_3)$ to be time variable (within the range of 0.0001 and 0.0004 s/m) to test our method's ability to resolve the time-varying wave slowness vector. For the wave function $f(t)$ we used the three-component seismogram recorded by station TA234A of USArray on 27 February 2010 and applied the appropriate time shifts, geometrical spreading, and radiation patterns to simulate a complex wavefield crossing our array with time-variable vector slowness. To implement the time-variable slowness we used the same method as described in Paper 1, which we will not repeat here for the sake of brevity. After constructing the synthetic seismograms, we applied a band-pass filter of 0.1–1.7 Hz. The smallest wavelength for these wavespeeds and frequency content is approximately 1.5 km. Therefore, the synthetic gradiometer had a maximum aperture of only 150 m, which adheres to the condition that the gradiometer have an aperture of no more than 10% of the smallest wavelength being analyzed. This condition minimizes the numerical errors associated with estimating the spatial derivatives (Langston, 2007c). We then use equations (32) through (34) to estimate the wave's direction and compare them to the known values of the wave direction (Fig. 2).

### Results of Synthetic Tests

For the first test, we estimated the wave direction of a synthetic, zero-noise signal (Fig. 2). Our method accurately estimates the known wave directions $\phi$, $\theta$, regardless of the component used to make the estimates. However, we note that there is an ambiguity of 180° in the estimation of the wave azimuth $\phi$. This ambiguity can be removed immediately either by using the gradiometric analysis of the vertical component data as shown in Paper 1, or by simply assuming one of the azimuth directions to the source.

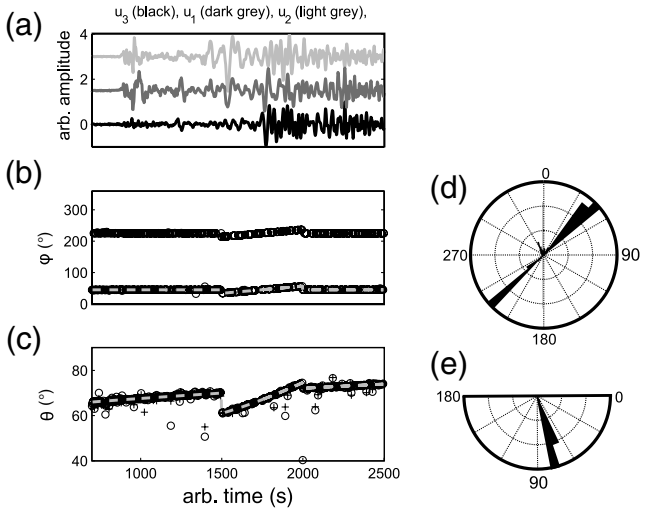


**Figure 2.** Numerical verification of wave direction estimations. The synthetic array was composed of fifteen recording stations in a roughly cubic arrangement with an aperture of 150 m. (a) The synthetic data as generated by equation (40). Note that we varied the wave direction as a function of time in order to illustrate that our method can resolve wave direction for each point on the seismogram. The three wave components $u_1$, $u_2$, $u_3$ are indicated, and offset for clarity. We show the seismograms for only the array's central station; however, for the array scale and wavespeeds used here, there is very little observable moveout. (b,c) Estimates of wave direction as calculated from equations (32) through (34), and the dashed light gray lines show the known value of wave direction for comparison. For the estimation of the direction $\phi$, we averaged the results at each time point for all three wave component derivatives (equation 32). Note that there is a 180° ambiguity in the estimation of the direction $\phi$, as the actual value of $\phi$ was $45 \pm 10°$. Because there are two ways to estimate the direction $\theta$ (equations 33 and 34) we show the result of the $\theta$ estimate for each equation. Specifically, the circles show the result for equation (33) and the plus signs show the result for equation (34). For each estimate of $\theta$ shown, we averaged the results at each time point for all three wave component derivatives, similar to the $\phi$ estimate. (d,e) The rose diagrams summarize the estimated wave directions by time averaging the direction estimates over the time window shown in the figure. The rose diagram clearly shows the 180° ambiguity in the estimate of the direction $\phi$.

Specifically, in Paper 1, the wave direction is estimated by using the $B_i$ , $i = 1, 2, 3$ parameters to estimate the component slowness directly. Simple geometry subsequently yields the wave direction. Regardless, this ambiguity does not exist when calculating the direction $\theta$ of the wavefield because it can only range between 0° and 180°.

## Effects of Noise on the Estimate of Wave Direction

Seismic gradiometry relies on highly correlated seismograms across the array. Furthermore, the model assumes that only one wave is traversing the array at any given time. Any phenomena that violates these two conditions can severely reduce the accuracy of the results (Poppeliers, 2010, 2011; Poppeliers *et al.*, 2013). Noise in the data can violate either of these conditions by (1) decorrelating the seismograms, in the case of random noise, or (2) having multiple waves traversing the array simultaneously, as would be the case for coherent noise such as microseism superposed on an earthquake signal. In this section, we explore both of these situations using simulations. We anticipated that noise in the data would negatively impact all of the wave parameter estimations. However, because the first step in the methods presented here is to obtain an accurate estimate of the wave direction, we focus on that first. Specifically, we add noise to a synthetic seismogram of known propagation direction and measure the degree to which the noise degrades the estimations of the wave directions using equations (32) through (34).

### Uncorrelated Noise

Uncorrelated noise in the seismogram refers to random fluctuations in amplitude or phase in a signal that is not due to any underlying physics of the wave model (e.g., instrument noise) and serves to decorrelate the seismograms in the array. This type of noise will be unique for each seismogram in the array. To test the effects of this type of noise on our results, we added random noise to each virtual seismometer in the array. To form the noise, we created a vector of random numbers normally distributed with a standard deviation of $0.5\Lambda$, in which $\Lambda$ is a constant that controls the root mean square (rms) amplitude of the noise signal. The noise signal is unique, and thus uncorrelated, for each signal recorded by the array. We performed four tests, with a progressively increasing amplitude of noise (Fig. 3).

This test illustrates that random noise results in a high degree of variance in the estimates of wave direction when the rms amplitude of the noise is greater than 2.5% the rms amplitude of the signal. Higher amplitudes of noise increase the degree of variance in both of the direction estimates, but the greatest effect is on the estimate of wave direction $\theta$. This is likely due to the fact that to estimate $\theta$, the $\phi$ must be used in the calculation (equations 33–34), which will also have noise-induced errors in it. Thus, it appears that the estimates of $\theta$ are approximately twice as sensitive to uncorrelated noise as the wave azimuth estimates.

### Correlated Noise

Here, we define correlated noise as any signal resulting from an actual physical phenomenon that may be correlated across the array and interferes with the signal that we are trying to analyze. Examples of this type of noise may include microseism or directional cultural noise. Our model of correlated noise is designed to simulate high-frequency surface waves. We constructed a sinusoidal signal (frequency = 0.25 Hz) that propagates across the array with an azimuth of $\theta = 285°$ from north and an incidence angle of $\phi = 0°$ from the horizontal (i.e., parallel to the ground surface) with a wavespeed of 4 km/s. To conduct the test, we added the noise signal to the original signal (similar to that shown in Fig. 3), for which the actual signal had a propagation direction of $\phi = 45$ and $\theta = 54$ degrees. The rms amplitude of the

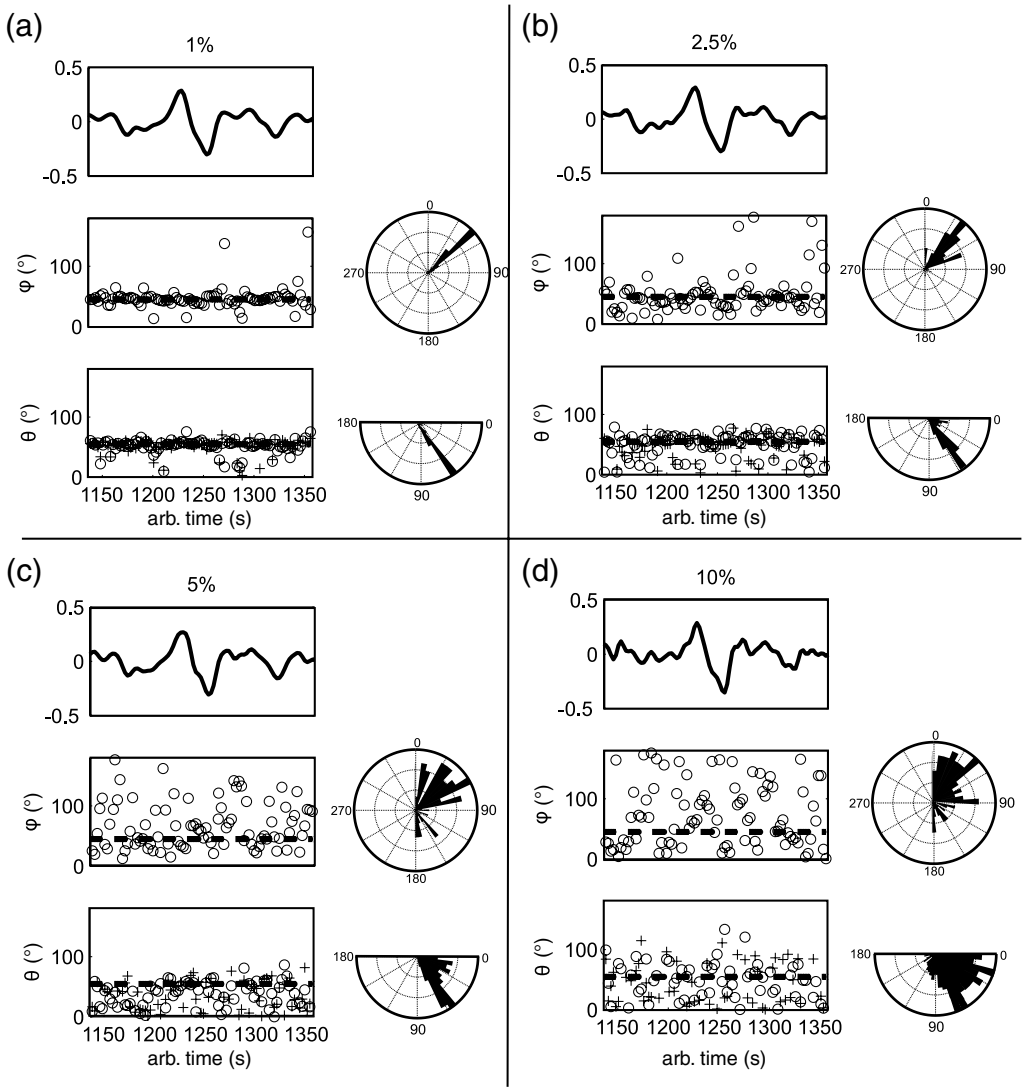


**Figure 3.** Estimates of propagation direction when random, uncorrelated noise is added to the synthetic seismogram. For this test, we used the same seismogram as shown in Figure 2, but windowed it in time and added uncorrelated, filtered noise to each seismogram prior to estimating the wave directions. The true wave directions are indicated by the heavy dashed lines. The rose diagrams are constructed using the entire signal shown here. For this case, we removed the 180° ambiguity by forcing the wave direction to always be in the same quadrant. For this figure, we averaged the results over all components similarly to Figure 2. Also, we show the estimates for the direction $\theta$ for both equations (33) and (34) using circles and plus signs, respectively. Panels (a), (b), (c), and (d) show the results for when the rms amplitude of noise is 1%, 2.5%, 5%, and 10% the rms amplitude of the actual signal, respectively.

signal varied from 0% to 200% of the rms amplitude of the noise. We then computed the resulting wave directions, averaged over the time interval of 1150 to 1350 s (which corresponds to the high amplitude portion of the signal shown in Fig. 2) and computed the standard deviation. Figure 4 shows the estimates of $\phi$ and $\theta$ as well as $\pm 1$ standard deviation about the mean of the estimated directions, estimated over the time window as a function of noise amplitude.

We make two main observations. First, as the amplitude of the noise increases relative to the signal, the estimate of the wave direction becomes less accurate, and the scatter (as measured by $\pm 1$ standard deviation) becomes greater. The second observation is that as the amplitude of the noise increases, the average wave direction estimate approaches that of the noise itself. As the amplitude of the noise continues to increase (greater than $\approx$50% of the signal), the uncertainty of the direction estimates actually decreases (less scatter) as the noise dominates and the signal is essentially ignored by the analysis. Also, the estimate of the wave direction $\phi$ appears to be more effected by noise than the estimate of $\theta$. This is surprising, as the estimate of $\theta$ requires an estimate of $\phi$, and directly contradicts the observations made in the previous noise test (Fig. 3).

## Discussion and Conclusions

The derivations that we present in this paper complete the mathematical description of 3D, three-component wave

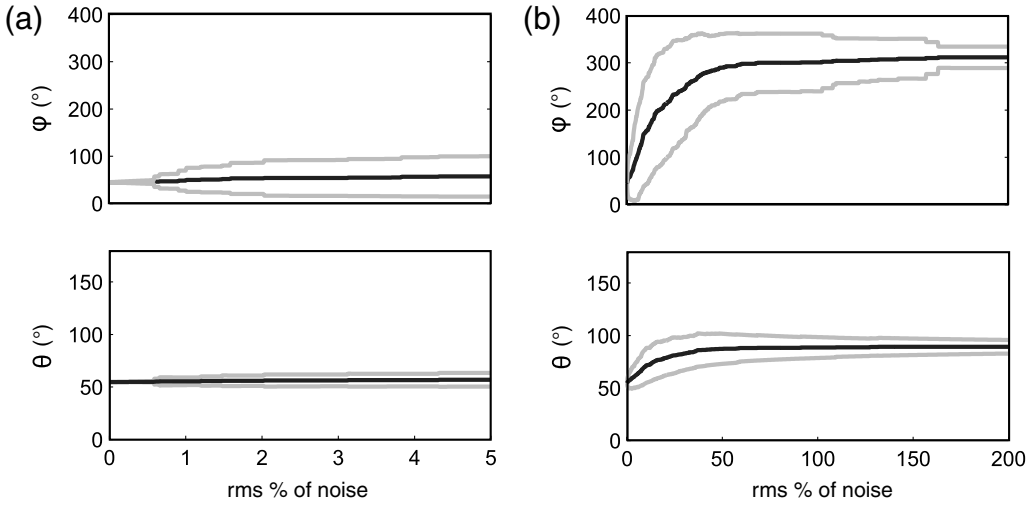


**Figure 4.** Noise test using correlated noise. The noise takes the form of a horizontally-traveling plane wave traversing the array at an azimuth of 285° from north. The noise is then added to the same signal as shown in Figure 3. After estimating the wave directions for each time point, we averaged over the entire time window (1150–1350 s, Figs. 1, 2) and calculated the mean and standard deviation about the mean. The mean of the estimated wave direction is shown by the black line. The scatter about the mean is shown by the gray lines and was calculated as $\pm 1$ standard deviation of the wave direction about the mean wave direction. Almost identical results were seen using any of the three wave components in equations (32) through (34). (a) When the noise has an rms amplitude of less than approximately two percent of the signal amplitude, there is only a small degree of scatter. (b) As the noise amplitude increases beyond approximately two percent of the signal amplitude, the scatter about the mean estimated wave directions significantly increases. As the noise amplitude continues to increase, the method returns the direction estimates of the noise itself.

gradiometry. In Paper 1 we developed a method to determine 3D wave attributes using a scalar wavefield. The results in that paper allowed us to estimate wavespeed and direction as well as a set of partial differential equations to estimate the radiation pattern for a scalar wavefield. The purpose of the work presented here is to build on this approach but use the polarized, three-component wavefield that is commonly recorded with seismic instrumentation. The main results that we obtained in this paper are (1) a mapping between the Cartesian-oriented spatial derivatives and the spherical derivatives and (2) a set of partial differential equations that relate the spherical derivatives of the polarized wavefield to the radiation patterns for all three body-wave types. These differential equations are likely the most important results of this paper. However, the solution to them is not trivial, and is the subject of current research efforts. Regardless, prior to estimating the body-wave radiation patterns, we require knowledge of the wave direction on a point-by-point basis for the portion of the seismogram of interest. Because of this necessity, we also derived a set of equations that gives a simple relationship between the Cartesian wavefield derivatives and the wave direction, although there is an 180° ambiguity with the wave direction $\phi$. The ambiguity can be resolved either by knowing the general direction of the incoming wavefield or by using the more complex gradiometric analysis as developed in Paper 1, which does not suffer from this ambiguity.

Because of the importance of knowing the wavefield direction and the relative simplicity of equations (32) through (33), we performed numerical tests to determine the robustness of estimating the wavefield direction from these equations. We also explored the effects of noise on the estimation of the wavefield direction, similar to our tests in Paper 1. In general, we found that equations (32) through (33) give fairly robust results for noise-free synthetic seismograms, but the results are quite sensitive to both uncorrelated and correlated noise. However, due to the small aperture of a gradiometer, it is virtually guaranteed that the seismograms be highly correlated across the array and thus we do not anticipate that uncorrelated noise will be a significant issue in an actual deployment. Rather, it is much more likely that correlated noise would be present. For example, a common source of correlated noise may be microseism superposing the wavefield of a discrete seismic event. Our numerical tests indicate that when the amplitude of the correlated noise is more than approximately two percent of the amplitude of the actual signal, there is a significant increase in the scatter about the mean estimated wave direction. Clearly, gradiometric analysis requires very high-quality data. In this regard, wave gradiometry is not as robust as conventional methods of seismic array processing, such as beam forming. However, one advantage that gradiometric analysis has over conventional array processing methods is its computational speed. The most computationally demanding aspect of the numerical results shown here was the matrix inversion to find the spatial derivatives. However, with only fifteen stations, this inversion was quite fast. Unless there were several hundreds of stations, we do not envision that solving equation (39) for the wave derivatives will be a significant bottleneck in this analysis. As the amplitude of the noise surpasses the amplitude of the signal, the analysis returns the direction of the noise itself, but with a high degree of scatter. This is not a surprising result, however, because the presence of a high

amplitude coherent noise source violates the single wavefield assumption of this method. For our testing method, we used synthetics calculated analytically via equation (40), but the gold standard test would analyze actual seismic data collected from an appropriately-scaled 3D array. However, as we know of no such deployment, we are forced to limit our tests to synthetic data. We suggest that the next step in this research is the deployment of an actual 3D array, or to conduct tests with more realistic synthetic data (for example, seismograms simulated by a finite-difference scheme) for testing the robustness of estimating wave directions, determining the seismic radiation patterns, and quantifying the effects of the wave reflecting off of the ground surface.

In our derivations, we assume a perfectly spherical wave model, and that all the coordinate systems are centered at the seismic source. The question, then, is how can the wavefield have time-variable wave parameters? We address this contradiction by claiming that the source can change positions with time, as will occur with seismic scattering or a finite rupture of a large fault system. This interpretation appeals to our physical sense, in that a given seismogram can contain arrivals from multiple sources. The gradiometric method places no inherent requirement that each seismic arrival have the same physical origin.

The potential applications of 3D gradiometry are numerous. For example, a small high-frequency gradiometer could be deployed as part of a program to monitor the effects of hydraulic fracturing as performed during petroleum extraction. Gradiometric analysis may be able to help monitor the frequency and directionality of microseismic events associated with the fracturing process. It may also be able to help resolve the fracture mechanism if we can develop a robust method to solve equations (35) through (37) for the body-wave radiation patterns. An additional potential application may be to the observation of rotational seismic waves. Typically, rotational seismic energy is estimated using a seismic array by estimating numerical derivatives and noting that

$$\vec{\omega} = \frac{1}{2}\nabla \times \vec{u}(\vec{x}), \tag{41}$$

for which $\vec{\omega}$ is a pseudovector representing the angle of the rigid rotation generated by the passage of a seismic wave (Cochard *et al.*, 2006). Rotational motions are usually observed about the $x_1$-, $x_2$-, and $x_3$-axis at the Earth's surface using either a 2D seismic array (e.g., Spudich *et al.*, 1995; Huang, 2003; Spudich and Fletcher, 2008) or directly with a rotational instrument (Takeo, 1998; Madziwa-Nussinov *et al.*, 2012) for which

$$\omega_1 = \frac{\partial u_3}{\partial u_2}, \tag{42}$$

$$\omega_2 = -\frac{\partial u_3}{\partial u_1}, \tag{43}$$

and

$$\omega_3 = \frac{1}{2}\left(\frac{\partial u_1}{\partial u_2} - \frac{\partial u_2}{\partial u_1}\right). \tag{44}$$

However, equations (41) through (44) give the rotational motions in Cartesian coordinate system about the $x_3$-axis. We suggest that by applying our map between the Cartesian derivatives and the spherical derivatives, one can express the rotational motions in spherical coordinate system. Thus, rotational motions in the seismic ray's natural ray-based coordinate system can be found. The result is that torsional-mode body waves can be observed on a 3D seismic array using conventional three-component instrumentation. Although the derivation of this is beyond the scope of this paper, we will be presenting the result in a forthcoming paper.

## Data and Resources

The seismogram used to make the synthetic data was downloaded from the Incorporated Research Institutions for Seismology (IRIS) Data Management System and is freely available.

## Acknowledgments

The authors acknowledge the very constructive and thorough comments offered by two anonymous reviewers, as well as the comments made by Associate Editor E. Chael. These reviews greatly improved the quality of this paper.

## References

Bodin, P., J. Gomberg, S. K. Singh, and M. Santoyo (1997). Dynamic deformations of shallow sediments in the Valley of Mexico, part I: 3D strains and rotations recorded on a seismic array, *Bull. Seismol. Soc. Am.* **87,** 528–539.

Cochard, A., H. Igel, B. Schuberth, W. Suryanto, A. Velikoseltsev, U. Schreiber, J. Wasserman, F. Scherbaum, and D. Vollmer (2006). Rotational motions in seismology: Theory, observation, simulation, in *Earthquake Source Asymmetry, Structural Media and Rotation Effects*, R. Teisseyre, M. Takeo, and E. Majewski (Editors), Springer-Verlag, Heidelberg, 391–411.

Gomberg, J., G. Pavlis, and P. Bodin (1999). The strain in the array is mainly in the plane (waves below ~1 Hz), *Bull. Seismol. Soc. Am.* **89,** 1428–1438.

Huang, B. S. (2003). Ground rotational motions of the 1991 Chi-Chi, Taiwan earthquake as inferred from dense array observations, *Geophys. Res. Lett.* **30,** no. 6, 1307–1310.

Langston, C. A. (2007a). Spatial gradient analysis for linear seismic arrays, *Bull. Seismol. Soc. Am.* **97,** no. 1B, 265–280, doi: 10.1785/0120060100.

Langston, C. A. (2007b). Wave gradiometry in two dimensions, *Bull. Seismol. Soc. Am.* **97,** no. 2, 401–416, doi: 10.1785/0120060138.

Langston, C. A. (2007c). Wave gradiometry in the time domain, *Bull. Seismol. Soc. Am.* **97,** no. 3, 926–933, doi: 10.1785/0120060152.

Langston, C. A., and C. Liang (2008). Gradiometry for polarized seismic waves, *J. Geophys. Res.* **113,** B08305, doi: 10.1029/2007JB005486.

Madziwa-Nussinov, T., K. Wagoner, P. Shore, C. R. Hutt, J. R. Eveans, N. Krishnan, and R. Cowsik (2012). Characteristics and response of a rotational seismometer to seismic signals, *Bull. Seismol. Soc. Am.* **102,** 563–573, doi: 10.1785/0120110166.

Poppeliers, C. (2010). Seismic wave gradiometry using the wavelet transform: Application to the analysis of complex surface waves recorded at the Glendora array, Sullivan, Indiana, USA, *Bull. Seismol. Soc. Am.* **100,** 1211–1224, doi: 10.1785/0120090304.

Poppeliers, C. (2011). Multiwavelet seismic-wave gradiometry, *Bull. Seismol. Soc. Am.* **101,** 2108–2121, doi: 10.1785/0120100226.

Poppeliers, C., P. Punoševac, and T. Bell (2013). Three-dimensional seismic-wave gradiometry for scalar waves, *Bull. Seismol. Soc. Am.* **103,** no. 4, doi: 10.1785/0120120224.

Spudich, P., and J. B. Fletcher (2008). Observation and prediction of dynamic ground strains, tilts, and torsions caused by the $M_w$ 6.0 2004 Parkfield, California, earthquake and aftershocks derived from UPSAR array observations, *Bull. Seismol. Soc. Am.* **98,** no. 4, 1898–1914.

Spudich, P., L. K. Steck, M. Hellweg, J. B. Fletcher, and L. M. Baker (1995). Transient stresses at Parkerfield, California, produced by the *M* 7.4 Landers Earthquake of June 28 1992: Observations from the UPSAR dense seismograph array, *J. Geophys. Res.* **100,** no. B1, 675–690.

Takeo, M. (1998). Ground rotational motions recorded in the near-source region of earthquakes, *Geophys. Res. Lett.* **25,** no. 6, 789–792.

## Appendix

Here, we present the details of the derivative calculations beginning with equations 19. Recall that relationship between spherical and Cartesian coordinates is given by

$$x_1 = r\sin\theta\sin\phi \qquad x_2 = r\sin\theta\cos\phi \qquad x_3 = r\cos\theta\,, \tag{A1}$$

and the relationship between Cartesian-based seismograms and the ray-based seismograms is

$$\begin{bmatrix} u_r \\ u_\phi \\ u_\theta \end{bmatrix} = \mathbf{R}_\theta\mathbf{R}_\phi \begin{bmatrix} u_1 \\ u_2 \\ u_3 \end{bmatrix}. \tag{A2}$$

Also, recall the following notation:

$$u_{i,j} = \frac{\partial u_i}{\partial x_j}. \tag{A3}$$

We first apply the product rule to equation (18) and then the chain rule to differentiate $\frac{\partial u_i}{\partial r}$:

$$\begin{aligned}\begin{bmatrix} u_{r,r} \\ u_{\phi,r} \\ u_{\theta,r} \end{bmatrix} &= \frac{\partial}{\partial r}\begin{bmatrix} u_r \\ u_\phi \\ u_\theta \end{bmatrix} = \mathbf{R}_\theta\mathbf{R}_\phi\frac{\partial}{\partial r}\begin{bmatrix} u_1 \\ u_2 \\ u_3 \end{bmatrix} = \mathbf{R}_\theta\mathbf{R}_\phi\begin{bmatrix} \frac{\partial u_1}{\partial r} \\ \frac{\partial u_2}{\partial r} \\ \frac{\partial u_3}{\partial r} \end{bmatrix} \\ &= \mathbf{R}_\theta\mathbf{R}_\phi\begin{bmatrix} \frac{\partial u_1}{\partial x_1}\frac{\partial x_1}{\partial r} + \frac{\partial u_1}{\partial x_2}\frac{\partial x_2}{\partial r} + \frac{\partial u_1}{\partial x_3}\frac{\partial x_3}{\partial r} \\ \frac{\partial u_2}{\partial x_1}\frac{\partial x_1}{\partial r} + \frac{\partial u_2}{\partial x_2}\frac{\partial x_2}{\partial r} + \frac{\partial u_2}{\partial x_3}\frac{\partial x_3}{\partial r} \\ \frac{\partial u_3}{\partial x_1}\frac{\partial x_1}{\partial r} + \frac{\partial u_3}{\partial x_2}\frac{\partial x_2}{\partial r} + \frac{\partial u_3}{\partial x_3}\frac{\partial x_3}{\partial r} \end{bmatrix}.\end{aligned} \tag{A4}$$

If we examine the first row, we can rewrite it as

$$u_{1,1}\frac{\partial x_1}{\partial r} + u_{1,2}\frac{\partial x_2}{\partial r} + u_{1,3}\frac{\partial x_3}{\partial r}$$

for which

$$\frac{\partial x_1}{\partial r} = \sin(\theta)\sin(\phi) \qquad \frac{\partial x_2}{\partial r} = \sin(\theta)\cos(\phi) \qquad \frac{\partial x_3}{\partial r} = \cos(\theta).$$

Similarly, we can obtain the next two rows, giving us

$$\begin{aligned}\begin{bmatrix} u_{r,r} \\ u_{\phi,r} \\ u_{\theta,r} \end{bmatrix} &= \mathbf{R}_\theta\mathbf{R}_\phi\begin{bmatrix} u_{1,1}\sin\theta\sin\phi + u_{1,2}\sin\theta\cos\phi + u_{1,3}\cos\theta \\ u_{2,1}\sin\theta\sin\phi + u_{2,2}\sin\theta\cos\phi + u_{2,3}\cos\theta \\ u_{3,1}\sin\theta\sin\phi + u_{3,2}\sin\theta\cos\phi + u_{3,3}\cos\theta \end{bmatrix} \\ &= \mathbf{R}_\theta\mathbf{R}_\phi\begin{bmatrix} u_{1,1} & u_{1,2} & u_{1,3} \\ u_{2,1} & u_{2,2} & u_{2,3} \\ u_{3,1} & u_{3,2} & u_{3,3} \end{bmatrix}\begin{bmatrix} \sin\phi\sin\theta \\ \cos\phi\sin\theta \\ \cos\theta \end{bmatrix}.\end{aligned} \tag{A5}$$

We proceed similarly for the derivative with respect to $\phi$

$$\begin{aligned}\begin{bmatrix} u_{r,\phi} \\ u_{\phi,\phi} \\ u_{\theta,\phi} \end{bmatrix} &= \frac{\partial}{\partial\phi}\begin{bmatrix} u_r \\ u_\phi \\ u_\theta \end{bmatrix} \\ &= \mathbf{R}_\theta\frac{\partial\mathbf{R}_\phi}{\partial\phi}\begin{bmatrix} u_1 \\ u_2 \\ u_3 \end{bmatrix} + \mathbf{R}_\theta\mathbf{R}_\phi\frac{\partial}{\partial\phi}\begin{bmatrix} u_1 \\ u_2 \\ u_3 \end{bmatrix} \\ &= \mathbf{R}_\theta\begin{bmatrix} \cos\phi & \sin\phi & 0 \\ -\sin\phi & \cos\phi & 0 \\ 0 & 0 & 0 \end{bmatrix}\begin{bmatrix} u_1 \\ u_2 \\ u_3 \end{bmatrix} + \mathbf{R}_\theta\mathbf{R}_\phi\begin{bmatrix} \frac{\partial u_1}{\partial\phi} \\ \frac{\partial u_2}{\partial\phi} \\ \frac{\partial u_3}{\partial\phi} \end{bmatrix} \\ &= \mathbf{R}_\theta\begin{bmatrix} \cos\phi & \sin\phi & 0 \\ -\sin\phi & \cos\phi & 0 \\ 0 & 0 & 0 \end{bmatrix}\begin{bmatrix} u_1 \\ u_2 \\ u_3 \end{bmatrix} \\ &\quad + \mathbf{R}_\theta\mathbf{R}_\phi\begin{bmatrix} \frac{\partial u_1}{\partial x_1}\frac{\partial x_1}{\partial\phi} + \frac{\partial u_1}{\partial x_2}\frac{\partial x_2}{\partial\phi} + \frac{\partial u_1}{\partial x_3}\frac{\partial x_3}{\partial\phi} \\ \frac{\partial u_2}{\partial x_1}\frac{\partial x_1}{\partial\phi} + \frac{\partial u_2}{\partial x_2}\frac{\partial x_2}{\partial\phi} + \frac{\partial u_2}{\partial x_3}\frac{\partial x_3}{\partial\phi} \\ \frac{\partial u_3}{\partial x_1}\frac{\partial x_1}{\partial\phi} + \frac{\partial u_3}{\partial x_2}\frac{\partial x_2}{\partial\phi} + \frac{\partial u_3}{\partial x_3}\frac{\partial x_3}{\partial\phi} \end{bmatrix} \\ &= \mathbf{R}_\theta\begin{bmatrix} \cos\phi & \sin\phi & 0 \\ -\sin\phi & \cos\phi & 0 \\ 0 & 0 & 0 \end{bmatrix}\begin{bmatrix} u_1 \\ u_2 \\ u_3 \end{bmatrix} \\ &\quad + \mathbf{R}_\theta\mathbf{R}_\phi\begin{bmatrix} u_{1,1}r\sin\theta\cos\phi - u_{1,2}r\sin\theta\sin\phi + 0 \\ u_{2,1}r\sin\theta\cos\phi - u_{2,2}r\sin\theta\sin\phi + 0 \\ u_{3,1}r\sin\theta\cos\phi - u_{3,2}r\sin\theta\sin\phi + 0 \end{bmatrix} \\ &= \mathbf{R}_\theta\begin{bmatrix} \cos\phi & \sin\phi & 0 \\ -\sin\phi & \cos\phi & 0 \\ 0 & 0 & 0 \end{bmatrix}\begin{bmatrix} u_1 \\ u_2 \\ u_3 \end{bmatrix} \\ &\quad + \mathbf{R}_\theta\mathbf{R}_\phi\begin{bmatrix} u_{1,1} & u_{1,2} & u_{1,3} \\ u_{2,1} & u_{2,2} & u_{2,3} \\ u_{3,1} & u_{3,2} & u_{3,3} \end{bmatrix}\begin{bmatrix} r\cos\phi\sin\theta \\ -r\sin\phi\sin\theta \\ 0 \end{bmatrix}\end{aligned} \tag{A6}$$

as well as for $\theta$

$$
\begin{aligned}
\begin{bmatrix} u_{r,\theta} \\ u_{\phi,\theta} \\ u_{\theta,\theta} \end{bmatrix} &= \frac{\partial}{\partial\theta}\begin{bmatrix} u_r \\ u_\phi \\ u_\theta \end{bmatrix} = \frac{\partial \mathbf{R}_\theta}{\partial\theta}\mathbf{R}_\phi \begin{bmatrix} u_1 \\ u_2 \\ u_3 \end{bmatrix} + \mathbf{R}_\theta \mathbf{R}_\phi \frac{\partial}{\partial\theta}\begin{bmatrix} u_1 \\ u_2 \\ u_3 \end{bmatrix} \\
&= \begin{bmatrix} -\sin\theta & 0 & -\cos\theta \\ 0 & 0 & 0 \\ \cos\theta & 0 & -\sin\theta \end{bmatrix} \mathbf{R}_\phi \begin{bmatrix} u_1 \\ u_2 \\ u_3 \end{bmatrix} + \mathbf{R}_\theta \mathbf{R}_\phi \begin{bmatrix} \frac{\partial u_1}{\partial\theta} \\ \frac{\partial u_2}{\partial\theta} \\ \frac{\partial u_3}{\partial\theta} \end{bmatrix} \\
&= \begin{bmatrix} -\sin\theta & 0 & -\cos\theta \\ 0 & 0 & 0 \\ \cos\theta & 0 & -\sin\theta \end{bmatrix} \mathbf{R}_\phi \begin{bmatrix} u_1 \\ u_2 \\ u_3 \end{bmatrix} \\
&\quad + \mathbf{R}_\theta \mathbf{R}_\phi \begin{bmatrix} \frac{\partial u_1}{\partial x_1}\frac{\partial x_1}{\partial\theta} + \frac{\partial u_1}{\partial x_2}\frac{\partial x_2}{\partial\theta} + \frac{\partial u_1}{\partial x_3}\frac{\partial x_3}{\partial\theta} \\ \frac{\partial u_2}{\partial x_1}\frac{\partial x_1}{\partial\theta} + \frac{\partial u_2}{\partial x_2}\frac{\partial x_2}{\partial\theta} + \frac{\partial u_2}{\partial x_3}\frac{\partial x_3}{\partial\theta} \\ \frac{\partial u_3}{\partial x_1}\frac{\partial x_1}{\partial\theta} + \frac{\partial u_3}{\partial x_2}\frac{\partial x_2}{\partial\theta} + \frac{\partial u_3}{\partial x_3}\frac{\partial x_3}{\partial\theta} \end{bmatrix} \\
&= \begin{bmatrix} -\sin\theta & 0 & -\cos\theta \\ 0 & 0 & 0 \\ \cos\theta & 0 & -\sin\theta \end{bmatrix} \mathbf{R}_\phi \begin{bmatrix} u_1 \\ u_2 \\ u_3 \end{bmatrix} \\
&\quad + \mathbf{R}_\theta \mathbf{R}_\phi \begin{bmatrix} u_{1,1} r\cos\theta\sin\phi + u_{1,2} r\cos\theta\cos\phi - u_{1,3} r\sin\theta \\ u_{2,1} r\cos\theta\sin\phi + u_{2,2} r\cos\theta\cos\phi - u_{2,3} r\sin\theta \\ u_{3,1} r\cos\theta\sin\phi + u_{3,2} r\cos\theta\cos\phi - u_{3,3} r\sin\theta \end{bmatrix} \\
&= \begin{bmatrix} -\sin\theta & 0 & -\cos\theta \\ 0 & 0 & 0 \\ \cos\theta & 0 & -\sin\theta \end{bmatrix} \mathbf{R}_\phi \begin{bmatrix} u_1 \\ u_2 \\ u_3 \end{bmatrix} \\
&\quad + \mathbf{R}_\theta \mathbf{R}_\phi \begin{bmatrix} u_{1,1} & u_{1,2} & u_{1,3} \\ u_{2,1} & u_{2,2} & u_{2,3} \\ u_{3,1} & u_{3,2} & u_{3,3} \end{bmatrix} \begin{bmatrix} r\sin\phi\cos\theta \\ r\cos\phi\cos\theta \\ -r\sin\theta \end{bmatrix}. \qquad \text{(A7)}
\end{aligned}
$$

Department of Chemistry and Physics
Georgia Regents University
Augusta, Georgia 30904
cpoppeli@gru.edu
(C.P.)

Department of Mathematics
Georgia Regents University
Augusta, Georgia 30904
ppunosev@gru.edu
(P.P.)

Manuscript received 7 May 2012